Atomistic analysis of the {10$\bar{1}$2} twin stability and growth in α-Ti

Enrique Martínez,[*] Laurent Capolungo, and Carlos N. Tomé

Material Science and Technology Division, MST-8, Los Alamos National Laboratory, Los Alamos, 87545 New Mexico, USA

{10$\bar{1}$2}⟨$\bar{1}$011⟩ twin is a prominent deformation mode in hexagonal close-packed materials. It is experimentally observed that twin interfaces are not flat entities, but characterized by kink pairs (KPs) of diverse heights. It has been shown that these kinks or facets delimit basal and prismatic planes. The nature of the defects constituting the facets prescribes their properties, in terms of stability and mobility, which relates to twin growth. In this work, we examine the basic features of such kinks in α-Ti from an atomistic modeling viewpoint. We analyze the response of the system with KPs varying in width and height upon normal and shear stresses and under pure bending conditions. We show that bending indeed modifies the interaction energy between kinks, which raises further questions about the nature of the defects. We calculate the nucleation and migration energy barrier for the twin depending on the applied shear stress, resulting in small values, which implies that small thermal energy suffices to activate twin growth. We observe a crossover in the stable height of the KP depending on the applied stress and its width: the wider the KP the higher the most stable. We have developed a twin thickening model that accounts for the thermal KP nucleation and the propagation of the kinks. We show how the model compares satisfactorily with molecular dynamics (MD) simulations. Finally, we have developed a kinetic Monte Carlo methodology to study twin growth, with much less computational burden than MD, that is able to explore the growth rate under a broader set of external conditions.

I. INTRODUCTION

Twinning is a prominent deformation mechanism in metals with hexagonal closed-packed (hcp) crystal symmetry. It provides an alternate deformation path to accommodate plasticity along the *c* axis. As opposed to slip on either pyramidal I or II systems, twinning induces a diffusionless transformation leading to the generation of reoriented volumes within the host crystal. In consequence, the effects of twinning on plastic deformation are more diverse and complex than those of slip alone. Over the past five decades or so, a vast body of literature has been generated in order to infer the role of twinning in both plastic deformation and microstructure evolution as well as the process(es) leading to the activation of twinning [1–7].

In this vein, focus has been placed on characterizing the nature of interfacial defects (i.e., disconnections, partial disclinations) mediating both nucleation and thickening of twin domains. With regards to the former and motivated by correlations shown between twin transmission events across grain boundaries and grain boundary character, a series of atomistic simulations have revealed the process by which a twin embryo can be formed at a grain boundary [8,9]. Further, using continuum based simulations of the plastic relaxation process in the neighborhood of twin domains, observations of the sequential twinning process across twin boundaries could be rationalized.

With regards to twin thickening, seminal contributions have introduced a means to describe the nature of interfacial defect mediating twin growth and diffusionless transformations in general. Using dichromatic patterns, it was shown that admissible defects at twin boundaries can be described as disconnections [3,4]. These essentially correspond to line defects inducing a net translation in the lattice with a translation vector having components parallel to the twinning shear direction (i.e., Burgers vector) and to the normal to the twinning plane. Both transmission electron microscopy (TEM) observations and atomistic simulations have then adopted this framework to describe the nature of interfacial defects as well as potential reactions between interfacial defects and bulk dislocations present at twin interfaces. For example, it is experimentally observed that among the several potential twin modes that could be active, {10$\bar{1}$2}⟨$\bar{1}$011⟩ twin is the most prominent in hcp materials such as Mg, Ti, or Zr [2,10,11]. Atomistic based quantifications of the activation barriers associated with the nucleation of interfacial defects on different twinning planes and simulations of the interaction between bulk dislocations and twin interfaces have both provided for credible explanations of the observed preference for {10$\bar{1}$2}⟨$\bar{1}$011⟩ twinning [12–14]. More recently, and on the basis of atomistic simulations, it has been argued that other defect types could be present at twin interfaces. Among others, a series of recent studies adopting a two-dimensional viewpoint constrained to the plane defined by the twinning shear direction and normal to the twinning plane, have revealed the existence of large facets (also called kinks) placing face to face basal planes and prismatic planes across the twin boundary (B/P or P/B interfaces) [7,15]. In parallel to this, a series of publications have suggested that these kinks, or other elementary defects at twin interfaces, are best described as dipoles of partial disclinations [16,17]. The rationale being that the reorientation of the lattice across the {10$\bar{1}$2}⟨$\bar{1}$011⟩ twin boundary leads to a net Frank vector of

_____
[*]enriquem@lanl.gov

$3.4°$. In the form of partial dipoles, these defects could induce both a net translation of the lattice across the twin interface as well as the necessary Frank vector. Trichromatic patterns were then introduced to further substantiate these proposals [12].

Despite these novel conceptual developments providing a complementary approach to describe interfacial defects, the core of those defects and their intrinsic dynamics are scarcely studied. Yet, these issues likely provide a path towards rationalizing the well-established experimental fact that twin thickening is remarkably faster and, apparently, insensitive to temperature in comparison to slip [18–20]. The present study aims at rationalizing these observations.

The kinetics, path, and temperature dependence for twin growth should be explicitly related to the very nature of the defects characterizing these kinks. While a significant body of work has been dedicated to the static analysis of interfacial defect characters, to the authors knowledge limited work has focused on the dynamics of interfacial defects. The present study relies on the use of atomistic and kinetic Monte Carlo (KMC) simulations to address three connected questions. First, it is known that twin boundaries are not flat, and the shape of twin boundaries makes it unlikely that the majority of interfacial defects are emitted from grain boundaries. As such, one expects twin thickening to be a two-step process whereby twin kink pairs (KPs) first appear on the twin boundary and then these newly generated interfacial defects migrate. Using atomistic simulations and leveraging the capabilities offered by the nudged-elastic band [21] (NEB) method to quantify minimum energy pathways (MEP), the activation barriers for KP nucleation and propagation are quantified. Based on this two-step process, a rate model for twin growth is developed. Second, while dichromatic patterns can reveal plausible interfacial defect types, the energetic cost associated with these can only be obtained via atomistic simulations. The second part of the study focuses on energetic considerations with the intent of rationalizing the simultaneous presence of interfacial defects of different character along the twin interface. Among others, the effects of curvature on KPs is also quantified. Finally, whilst anchoring the reasoning in the realm of transition state theory, a first attempt is made to elucidate the apparent lack of temperature sensitivity associated with twinning.

II. METHODOLOGY

Molecular static (MS) and molecular dynamics (MD) simulations have been performed with the LAMMPS code [22] to analyze the energetic properties of a $\{10\bar{1}2\}\langle\bar{1}011\rangle$ twin depending on its atomic structure and the boundary conditions. We have also studied the MEP for the nucleation and the growth of the twin KP. A fully periodic cell was built with directions $\langle10\bar{1}0\rangle$, $\langle01\bar{1}1\rangle$, and $\langle0\bar{1}11\rangle$ for the lower grain and $\langle\bar{1}010\rangle$, $\langle01\bar{1}1\rangle$, and $\langle01\bar{1}\bar{1}\rangle$ for the upper grain, which generates two $\{10\bar{1}2\}$ twin boundaries in the system. The dimensions of this periodic cell were $0.29 \times 34.8 \times 45.8$ nm^3. Although constrained to a quasi-two dimensional configuration, we shall see how much can be learned on the system dynamics. We use the first of the three embedded atom method (EAM) potentials developed by Mendelev *et al.* [23] for α-Ti. Minimizations were performed using a conjugate gradient algorithm with a tolerance in forces of 10^{-4} eV/Å. To generate the KP (green)
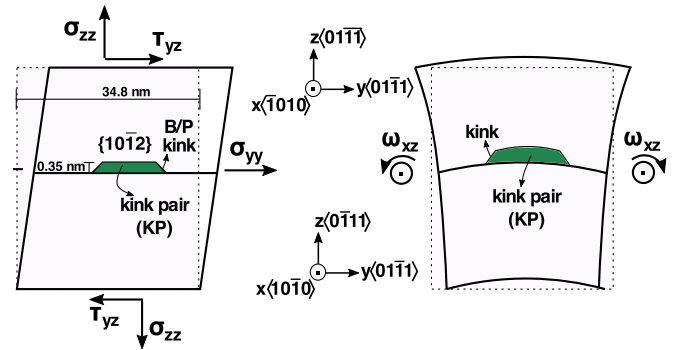

FIG. 1. Sketch of the sample orientation, twin KP (green), and applied stresses and rotations used in this study.

area in Fig. 1), a region of the sample close to the twin and in the upper grain was removed and filled with atoms with the orientation of the lower grain, such that the number of atoms remains constant. Both the height in z and the length in y of the KP were varied to compute formation energies.

Two distinct sets of boundary conditions were used. First, normal stresses were applied on the y and z directions (σ_{yy} and σ_{zz}), and shear in yz (σ_{yz}), i.e., simulations were stress-controlled. Second, to assess the role of curvature fields on the nucleation and propagation of KPs, the sample was subjected to pure bending in the yz plane (ω_{xz}). In this case, the periodic boundary conditions on y and z were dropped. A region of atoms close to the sample edges normal to the y direction was selected and displaced following $u_y = a + bz^2$. The displaced atoms were allowed to relax in the x and z directions but not in the y. Figure 2 shows the atomic structure of a KP of 6.9 nm in width relaxed at zero pressure. Upon relaxation of the structure the angle between basal planes in upper and lower grains results in 86.2°, close to the theoretical 85.22°.

III. RESULTS AND DISCUSSION

A. Kink pair formation and propagation process

We first focus on the generation of KPs from a perfect twin interface. In this section the KP consists of a dipole of $b_{2/2}$ disconnections separated by a distance w, which is varied. The
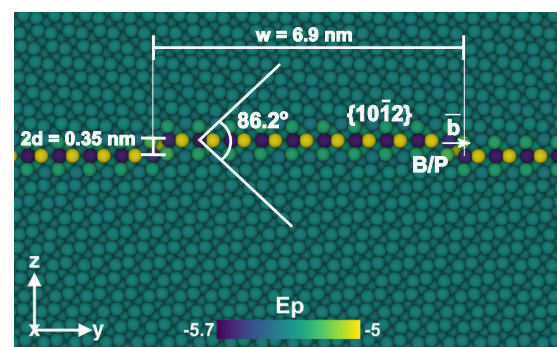

FIG. 2. Atomistic detail of the structure of the $\{10\bar{1}2\}$ twin. Atoms are colored according to their potential energy. The angle between basal planes results in 86.2°. The KP is bounded by basal/prismatic (B/P) interfaces. The distance between B/P interfaces is 6.9 nm.
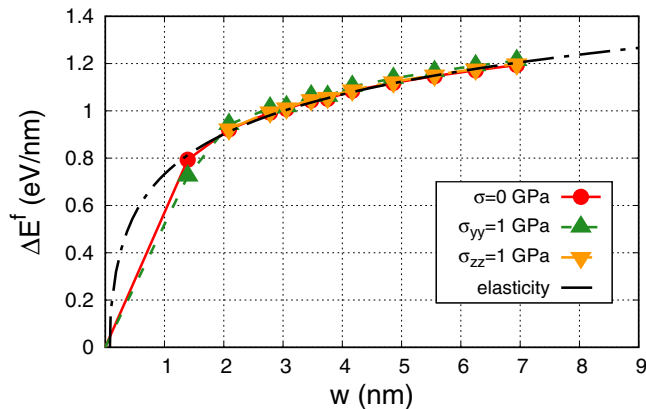
FIG. 3. Formation energy of the twin KPs depending on the distance between the B/P kinks and the applied normal stress.

FIG. 4. Formation energy of the twin KP depending on the distance between the B/P kinks and the applied shear stress.

excess energy of formation, $\Delta E^f(w)$, of the system containing these dipoles, in comparison with a domain of equal size containing a perfectly flat twin boundary, can be expressed as

$$\Delta E_0^f(w) = 2E_{b2/2}^{\text{core}} + E_{b2/2}^{\text{int}}(w), \qquad (1)$$

where $E_{b2/2}^{\text{core}}$ and $E_{b2/2}^{\text{int}}$ denote the core energy of an individual $b_{2/2}$ disconnection and the elastic interaction energy between the disconnections, respectively.

Figure 3 presents the formation energy ($\Delta E = E_{\text{KP}} - E_{\text{FLAT}}$, with E_{KP} the energy of the system with the KP and E_{FLAT} the energy of the system with a flat twin boundary) at zero pressure and applying stresses $\sigma_{yy} = -1$ GPa or $\sigma_{zz} = -1$ GPa (compressive stresses). We observe that the formation energy is fairly independent of these boundary conditions.

Following MacKain *et al.* [24], we could estimate the interaction energy assuming the presence of a dislocation dipole, which neglecting image interactions is given by

$$\Delta E_{b2/2}^{\text{int}}(w) = \frac{1}{4\pi}\kappa b^2 \ln\left(\frac{w}{r_c}\right), \qquad (2)$$

and therefore

$$\Delta E_0^f(w) = \frac{1}{4\pi}\kappa b^2 \ln\left(\frac{w}{r_c}\right) + 2E_{b2/2}^{\text{core}}, \qquad (3)$$

where κ is a constant that depends on the elastic constants and the disconnection orientation [24,25], b is the dislocation Burgers vector, equal to $b_{2/2}$ in this case with $b_{2/2} = 0.05624$ nm, w is the distance between kinks and r_c is a minimum critical radius. Fitting this relation to the atomistic data at zero stress we estimate $\kappa = 154.6$ GPa, $r_c = 0.23$ nm and a core energy per unit length of $E_{b2/2}^{\text{core}} = 0.188$ eV/nm.

Figure 4 shows the results when σ_{yz} shear stress is applied. The figure displays the formation energy of the KP depending on the separation between B/P interfaces. In this case, a significant variation in the energy is observed as a function of the applied stress. A maximum in some of the formation energy curves is observed, beyond which the KP will tend to grow to lower the system energy. When stress is applied, an extra energy term needs to be considered in the expression of
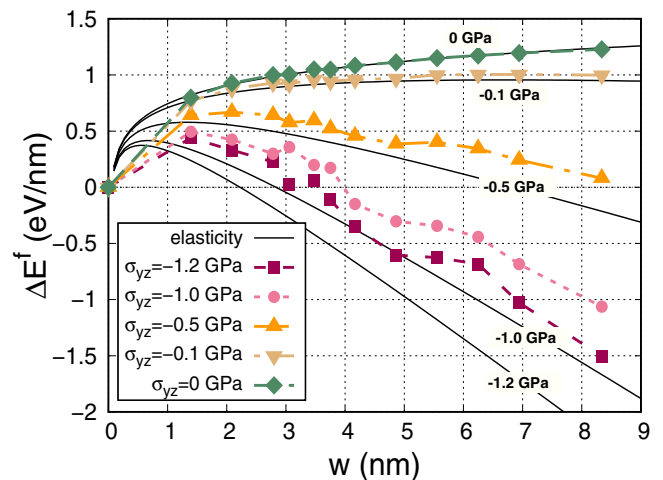
the formation energy as the work done by the external forces in the nucleation process, such that

$$\Delta E^f(w, \sigma_{yz}) = \frac{1}{4\pi}\kappa b^2 \ln\left(\frac{w}{r_c}\right) + 2E_{b2/2}^{\text{core}} - \sigma_{yz}bw. \quad (4)$$

The values obtained through this elastic approach are also presented in Fig. 4 as solid black lines. The slight discrepancies, mostly at high stresses, are due to two main reasons: (i) the image effects appearing in the atomistic simulations and not considered in the elastic solution and (ii) the fact that the nature of the defect does not have purely dislocation character (as we shall see later), which might add extra terms in the work done to nucleate the KP.

Figure 5(a) shows the MEP for a KP of 1.39 nm in width to nucleate from a flat twin boundary depending on the applied shear stress. The first saddle point is the Peierls barrier for nucleation, that clearly depends on stress. The second barrier is the Peierls energy barrier for the kink to glide. For stresses lower than $\sigma_{yz} = -1.2$ GPa, the barrier from the nucleated configuration back to the flat twin interface is lower than the barrier for the twin to grow, which indicates that those configurations are unstable and the KP will tend to shrink. On the other hand, for $\sigma_{yz} = -1.2$ GPa, we observe the opposite trend, which will lead to the preferential growth of the KP. Figure 5(b) shows the Peierls barriers for nucleation as a function of applied stress. We have expanded the activation enthalpy in terms of an activation potential energy and a linear relation on the stress, $\Delta H = \Delta E - \sigma_{yz}v_a$. The data given by the NEB calculations show a quadratic relation of ΔH with stress. If we assume that v_a does not depend on stress, we have

$$\frac{\partial \Delta H}{\partial \sigma_{yz}} = \frac{\partial \Delta E}{\partial \sigma_{yz}} - v_a = \beta\sigma_{yz} - v_a. \qquad (5)$$

From the fit we obtain a value of $\beta = 4.42 \times 10^{-5}$ nm³ nm⁻¹ MPa⁻¹ and an activation volume $v_a = 0.051$ nm³ nm⁻¹, values given per unit length of the KP in the x direction (see Fig. 1). A linear approximation neglecting the quadratic term ($\beta \approx 0$) is also shown in the figure. Note
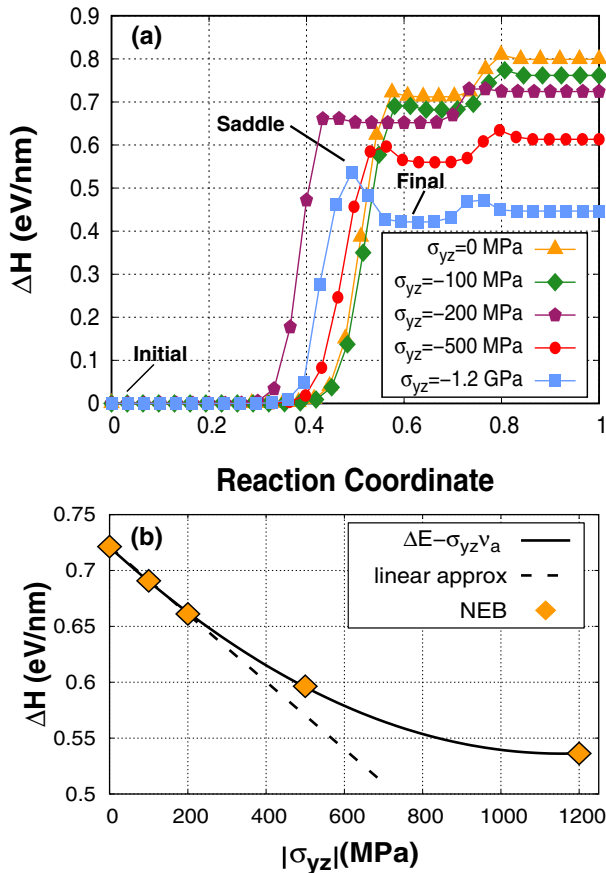
FIG. 5. (a) Potential energy barrier (Peierls potential) for the nucleation and growth of a twin KP depending on the applied shear stress. (b) Nucleation barrier with respect to applied stress in absolute value. NEB data fitted with a quadratic relation, $\Delta H = \Delta E - \sigma_{yz} v_a$, where ΔE is the potential energy barrier that depends on stress, and v_a is an activation volume. The dashed line is a linear fit to the data valid at low stress.
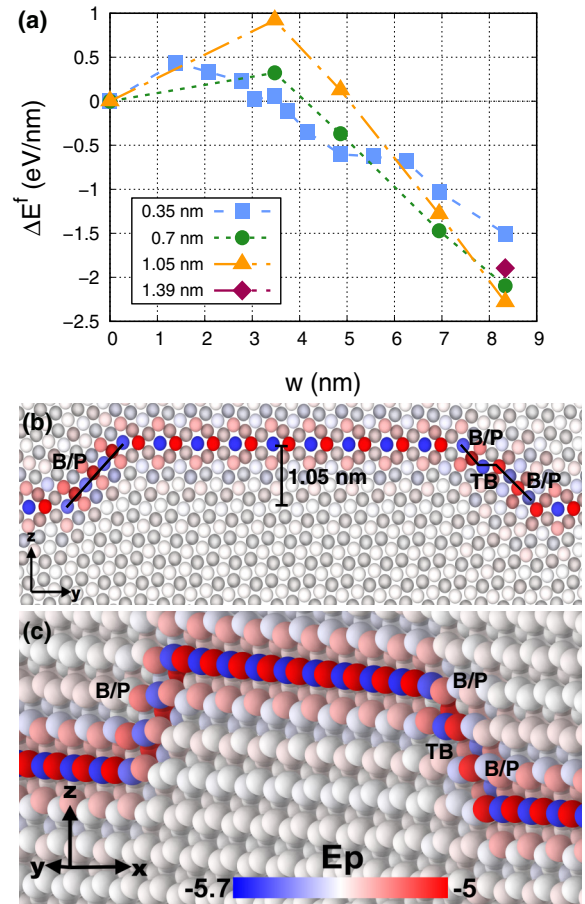

FIG. 6. (a) Formation energy depending on KP height and width at a $\sigma_{yz} = -1.2$ GPa. (b) and (c) Atomistic structure of a KP of 4.86 nm in width and 1.05 nm in height. B/P stands for basal/prismatic and TB for twin boundary. Atoms are colored according to their potential energy.

that the NEB calculations were performed at constant volume, once the desired stress was reached. We have not observed any noticeable deviation in the target stresses during these simulations.

B. Nature and coexistence of interfacial defects

The second point of interest concerns the defect configurations that could coexist at twin interfaces. To this end, we have studied the effect of the KP height in the formation energy. Figure 6(a) shows the formation energy, where we observe that for low KP widths the higher the KP the larger the formation energy, and therefore, less energetically favorable. More interestingly, we note a crossover in the curves for different heights. The configuration with a KP of height 0.7 nm becomes more favorable than the 0.35 nm at around a width of ∼5.5 nm. The configuration with a KP of 1.05 nm becomes more stable than the 0.35 nm KP at around ∼6 nm. We have also tested a height of 1.39 nm with a KP width of 8.3 nm. It is found that the 1.39 nm high KP is more stable than the original 0.35 nm KP but less favorable than 0.7 and 1.05 nm. Furthermore,

we also note that there is a crossover between the 0.7 nm height and the 1.05 nm. The latter becomes more stable at around ∼7.5 nm. These results imply that an optimal height-to-width ratio exists. As a general trend, the larger the width the higher the most stable KP. This relationship between height and width might be a plausible explanation to the experimental results in which different heights larger than the minimal 0.35 nm are observed. Also note that this relationship will depend on the applied stress. Our results indicate that the larger the stress the shorter the width required for the crossover to take place. Figures 6(b) and 6(c) show the atomic configuration of a KP of height 1.05 nm and width of 4.86 nm. The atoms are colored according to their potential energy. We observe that one of the B/P interfaces is flat (on the left), while the other shows a step, i.e., a twin boundary (TB) between B/P kinks (on the right, hereafter rugged configuration).

To gain further understanding on the structure of the B/P kink, we have perturbed the rugged configuration at $\sigma_{yz} = -1.2$ GPa with the goal of taking the system to a nearby minimum. We have selected a region around the rugged configuration and randomly displaced the enclosed atoms sampling uniformly from $[-0.5 : 0.5]$ Å. Once the atomic positions
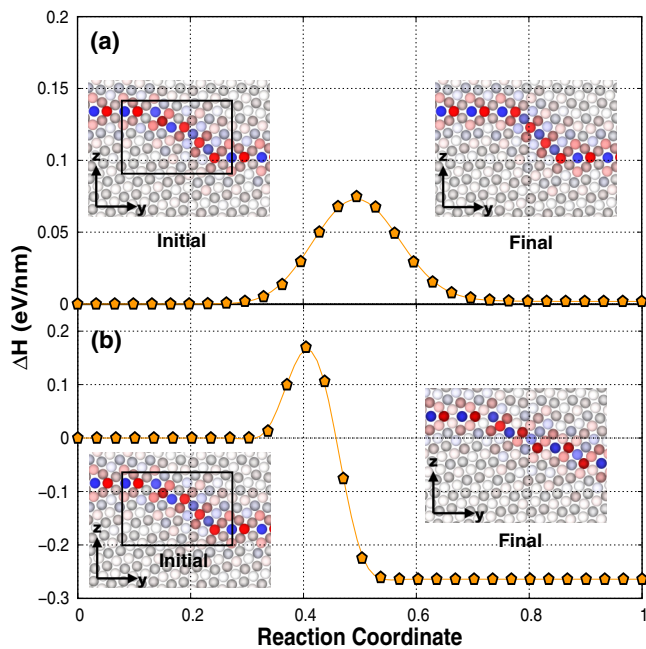
FIG. 7. Minimum energy path at a $\sigma_{yz} = -1.2$ GPa from the rugged configuration originally found to (a) flat B/P interface and (b) two-step interface. The rectangle in the initial atomic configuration shows the region where the atoms were randomly displaced. Atoms are colored according to their potential energy with the same scale as in Fig. 6.
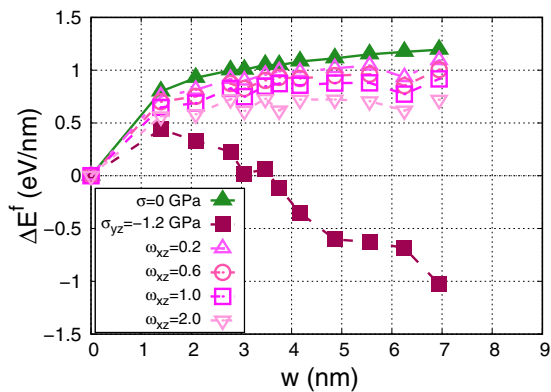

FIG. 8. Formation energy of the twin KP depending on the distance between the B/P kinks and the applied curvature. For comparison, the formation energies of the KP for $\sigma_{yz} = -1.2$ GPa and $\sigma = 0$ GPa are also shown.

are perturbed, the system is minimized again with the same settings as originally. A total of one hundred perturbations were tested and three main final configurations were found: the initial rugged configuration, a flat configuration and a two-step configuration, as shown in the insets of Fig. 7. Once we have the new structures, we have analyzed the MEP through NEB calculations. Figure 7 shows the results, with Fig. 7(a) presenting the MEP to go from the rugged configuration to the flat configuration and Fig. 7(b) depicts the path between the rugged and two-step configurations. First, we readily see [Fig. 7(a)] that the energy of the rugged configuration and the flat interface is virtually the same (less than 1.7 meV/nm). Second, the energy barrier between both configurations is extremely small (0.075 eV/nm) and therefore, both configurations will coexist at equal probabilities at finite temperature. The flat kink is usually related to the existence of a disclination dipole, while the stepped configuration is usually associated to the presence of a disconnection. These calculations show that both configurations are comparable in energy. On the other hand, the transition from the rugged configuration to the two-step configuration shows a slight reduction in energy of about 0.26 eV/nm, with a somehow larger activation energy, still of only 0.17 eV/nm. This last two-step configuration (disconnectionlike) is therefore the most stable among the ones that we have found.

To assess the disclination content of interfacial defects, we have also analyzed the effect of pure bending on the formation energy of the KP. Figure 8 shows the results for different degrees of rotation, as imposed by the displacements $u_y = a + b z^2$ and the atomic relaxations in the x and z directions.

Upon relaxation the imposed normal strain $\epsilon_{yy} \approx -0.024$ in the compressive side and $\epsilon_{yy} \approx 0.029$ in the tensile region. We observe that these rotations modify the formation energy of the kink, i.e., they do work when the KPs are nucleated, as in the case of shear stress described in Eq. 4. However, contrary to the shear stress, rotations do not lead to any apparent maximum or change in sign of the formation energy by themselves, i.e., there will not be spontaneous growth of the KP under pure bending boundary conditions. The fact that indeed the formation energy changes upon pure bending implies that defects at the B/P interfaces are complex in nature probably beyond simple disconnections since dislocations should not interact with curvature.

As described above, the traditional description of a kink involves a shear and a shuffle, which have been mapped to the presence of a disconnection, characterized by a Burgers vector and a step height. It has been recently shown that the interaction field between kinks follows a logarithmic law as the one derived from dislocation theory [24]. Our results shown in Figs. 3 and 4 also follow a logarithmic relation, which seems to imply the presence of a dislocation dipole. However, the interaction energy also follows a logarithmic-like function when curvature is applied, with such energy depending on the curvature value (see Fig. 8). This might indicate that disconnections might not suffice to model kinks. Disclination dipoles should respond to applied curvature, but the given relation to the curvature is mainly unknown [26].

C. Consequences of kink pair nucleation events on strain rate sensitivity

1. Twin thickening rate model

{10$\bar{1}$2}⟨$\bar{1}$011⟩ twins thicken by the nucleation of a KP and the propagation of the kinks upon the action of an external stress (see Fig. 9). This model assumes that the probability of nucleating KPs with the minimum height h is much larger than any larger height. This process is analog to the thermally activated glide of dislocations [27,28] and can be described as follows.
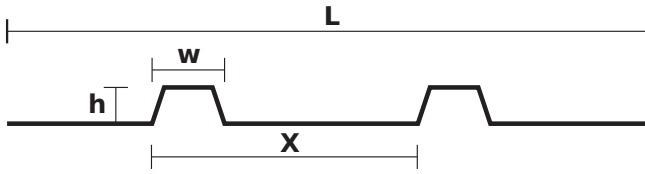
FIG. 9. Sketch showing the KP nucleation event in a twin thickening process and the relevant parameters used in the derivation of the twin thickening rate.

The total time for the twin to thicken by h is the time for the KP to nucleate plus the time for the kinks to propagate half their mean free path, $t = t_N + t_P$. In term of the rates, this total time can be written as

$$t = \frac{1}{\Gamma_N} + \frac{1}{\Gamma_P} = \frac{\Gamma_N + \Gamma_P}{\Gamma_N \Gamma_P}, \qquad (6)$$

where Γ_N is the number of nucleations per unit time and Γ_P is the rate for the kink to propagate until it annihilates with an opposite kink. Hence the velocity for the twin to grow is

$$v = \frac{h}{t} = h \frac{\Gamma_N \Gamma_P}{\Gamma_N + \Gamma_P}. \qquad (7)$$

In the framework of transition state theory (TST), the nucleation rate can be written as

$$\Gamma_N = \frac{v_0 X(\sigma, T)}{w^*(\sigma)} \exp\left(-\frac{\Delta G(\sigma, T)}{k_B T}\right), \qquad (8)$$

where v_0 is an attempt frequency, $X(\sigma, T)$ is the kink mean free path, $w^*(\sigma)$ is the critical width of the KP and ΔG is the activation Gibbs free energy. The critical width of the KP is the maximum in the formation energy (Fig. 4) and can be obtained differentiating Eq. 4 with respect to w and setting the derivative to zero:

$$\frac{\partial \Delta E^f(w, \sigma)}{\partial w} = \frac{1}{4\pi} \kappa b^2 \frac{1}{w} - \sigma b = 0, \qquad (9)$$

thus the critical width is

$$w^* = \frac{1}{4\pi} \frac{\kappa b}{\sigma}. \qquad (10)$$

Substituting in Eq. (8) results in

$$\Gamma_N = \frac{4\pi v_0 \sigma X(\sigma, T)}{\kappa b} \exp\left(-\frac{\Delta G(\sigma, T)}{k_B T}\right). \qquad (11)$$

The dependence of the kink mean free path with the applied stress and temperature is less clear and will be fitted from MD simulations. There is in the literature a square root dependence of X with stress [29], although no information could be found about the dependence on temperature. We will fit a function of the type $X(\sigma, T) \propto f(\sigma) g(T)$ to the MD data to obtain an empirical relation valid for the system at hand.

As it was shown in Fig. 5, the enthalpy barriers for the kinks to propagate are much smaller than the nucleation barrier. Thus the kink propagation can be assumed to happen in a phonon drag regime. In this regime, the propagation rate can be written as

$$\Gamma_P = \frac{2v_k}{X(\sigma, T) + w^*} \approx \frac{2v_k}{X(\sigma, T)} = \frac{2b\sigma}{X(\sigma, T) B_k}, \qquad (12)$$

where we assume $X(\sigma) \gg w^*$. v_k is the kink velocity, which in the viscous regime can be written as $v_k = \frac{b\sigma}{B_k}$, where B_k is a drag coefficient. Substituting the rates in the expression for the growth velocity, we obtain

$$v = h \frac{\frac{8\pi v_0 \sigma}{\kappa B_k} \exp\left(-\frac{\Delta G(\sigma, T)}{k_B T}\right)}{\frac{2b}{X(\sigma, T) B_k} + \frac{4\pi v_0 X(\sigma, T)}{\kappa b} \exp\left(-\frac{\Delta G(\sigma, T)}{k_B T}\right)}, \qquad (13)$$

which is a general expression for the thickening velocity of the twin. The shear strain rate can then be obtained:

$$\dot{\gamma} = \arctan\left(\frac{b}{h}\right) \frac{v}{h} \approx \frac{vb}{h^2}$$

$$= \frac{8\pi b v_0 \sigma}{h\kappa B_k} \frac{\exp\left(-\frac{\Delta G(\sigma, T)}{k_B T}\right)}{\frac{2b}{X(\sigma, T) B_k} + \frac{4\pi v_0 X(\sigma, T)}{\kappa b} \exp\left(-\frac{\Delta G(\sigma, T)}{k_B T}\right)}. \qquad (14)$$

It is worth showing the limit at which the propagation rate is much larger than the nucleation rate ($\Gamma_P \gg \Gamma_N$). In this limit, the total time for the twin to grow would be just the nucleation time, $t = t_N = \frac{1}{\Gamma_N}$. Therefore the velocity of the twin can be written as

$$v = h \frac{4\pi v_0 \sigma X(\sigma, T)}{\kappa b} \exp\left(-\frac{\Delta G(\sigma, T)}{k_B T}\right), \qquad (15)$$

and then the strain rate

$$\dot{\gamma} = \frac{4\pi v_0 \sigma X(\sigma, T)}{\kappa h} \exp\left(-\frac{\Delta G(\sigma, T)}{k_B T}\right), \qquad (16)$$

which is similar to the expression developed by Luque *et al.* in Ref. [30]. Also important to highlight is the fact that this expression is valid in three dimensions, provided that geometric considerations are taken into account along with the orientation dependence of the drag coefficient.

2. Molecular dynamics simulations

As mentioned above, MD simulations have been performed to test the twin thickening model developed above and to find specific parameters for the $\{10\bar{1}2\}\langle\bar{1}011\rangle$ twin in α-Ti. Hence we have set up MD simulations in the NPT ensemble with different levels of σ_{yz} and temperature and computed the shear strain rate, which will be, in general, larger than in traditional experimental tests due to the MD timescale limitation [31].

Assuming a Kocks relation for the activation Gibbs free energy [32] $\Delta G(\sigma, T) = \Delta F[1 - (\frac{\sigma_{yz}}{\sigma_{yz}^0})^p]^q$ and further considering $p = q = 1$, the functional form we have fitted from MD results was the following:

$$\dot{\gamma} = K \frac{\sigma_{yz}^{(1+\alpha)}}{T^\delta} \exp\left(-\frac{\Delta F\left[1 - \left(\frac{\sigma_{yz}}{\sigma_{yz}^0}\right)\right]}{k_B T}\right), \qquad (17)$$

where α and δ are fitting parameters coming from the functional form of $X(\sigma, T)$, K is a constant depending just on material parameters, ΔF is the Helmholtz free energy, and σ_{yz}^0 is a critical resolved shear stress that nullifies the activation barrier. The results are shown in Fig. 10, where the dependence of the shear strain rate with shear stress [Fig. 10(a)] and temperature [Fig. 10(b)] are shown. Dots are MD results while lines are best fits from Eq. (17) to the MD data. We observe that in both
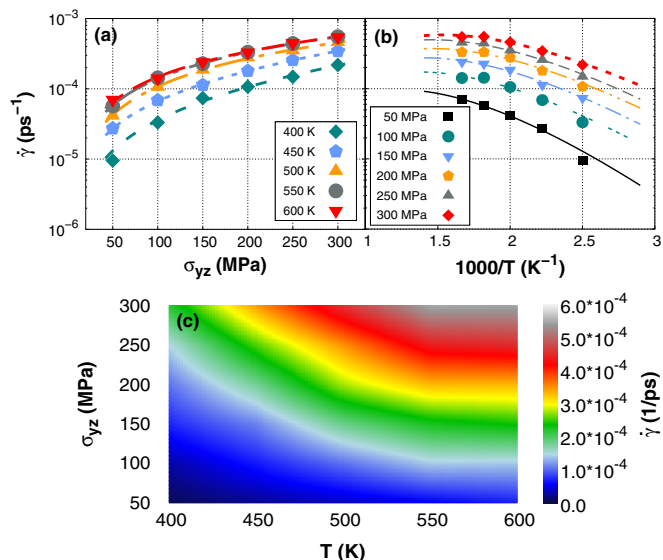
FIG. 10. Twin thickening rate depending on (a) shear stress, and (b) temperature. (c) 2D map of the twin thickening rate as given by MD simulations as a function of both temperature and stress.

cases the agreement is remarkable, validating the theoretical model developed in the previous section. This means that the ΔF can be assumed constant with respect to the applied stress, which, in turn, implies that the activation volume is constant. Hence we can write

$$-\frac{\partial \Delta G}{\partial \sigma_{yz}} = \frac{\Delta F}{\sigma_{yz}^0} = -\frac{\partial \Delta E}{\partial \sigma_{yz}} + v_a^* + T\frac{\partial \Delta S}{\partial \sigma_{yz}}, \quad (18)$$

and therefore, assuming that the functional form of ΔH is quadratic in σ_{yz} as given by the NEB calculations above,

$$\frac{\partial \Delta E}{\partial \sigma_{yz}} = T\frac{\partial \Delta S}{\partial \sigma_{yz}} = \beta^*\sigma_{yz}, \quad (19)$$

which implies that the functional form of the entropy can be written as $\Delta S = \frac{1}{T}[\frac{\beta^*}{2}\sigma_{yz}^2 + C_1]$, where C_1 is an integration constant that equals zero. Moreover, to first order, we can assume that the β obtained from the MS simulations is a good approximation to β^* ($\beta^* \approx \beta$). We can also conclude that $\Delta G(\sigma, T)$ does not depend on temperature, implying that TST holds, although not its harmonic approximation (HTST). Figure 10(c) shows a two-dimensional map with the rates as obtained with MD that we shall compare with the KMC results in the following, while Fig. 11 is a three-dimensional plot showing the prediction from Eq. (17) compared to MD data. The values of the fit are given in Table I. We note that the value for α is small, which indicates that the dependence of the mean free path between kinks depends only weakly on stress. On the other hand, we find a large value of δ implying a strong dependence on temperature. The fact that experimentally the temperature sensitivity seems to be small [18] is probably due to the fact that the effective activation barrier is low and the exponential dependence dominates, which is the case in the temperature range explored in this work. Unfortunately, direct comparison with experiments is not straightforward since they would include the twin nucleation rate, which is not part of this study. Also worth mentioning is the value of
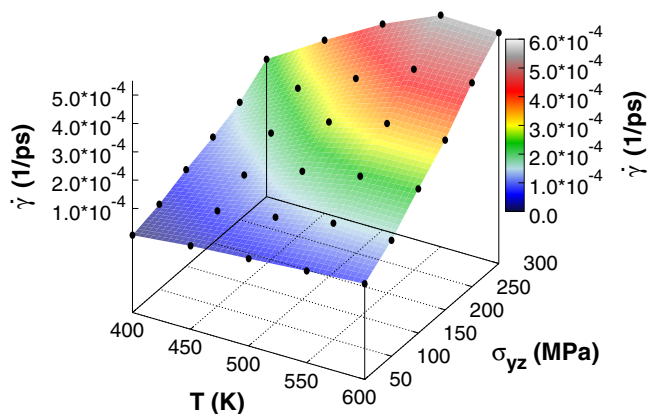

FIG. 11. Comparison between the MD data (black dots) and Eq. (17) (colored surface).

the activation barrier, $\Delta F = 0.886$ eV/nm, which, although close, is slightly larger than the value obtained using NEB at zero stress ($\Delta E_{\sigma_{yz}=0} = 0.721$ eV/nm). The same applies for the activation volume, in the case of fitting values to MD data we obtain $v_a^* = 0.077$ nm^3/nm, which compares to $v_a = 0.051$nm^3/nm given by the NEB simulations. We note that the values obtained from MD are averages over a different number of mechanisms involved in the thickening process as opposed to a single mechanism analyzed in the static calculations of Sec. III A, which results in the observed deviations.

Using the values for ΔF, v_a^*, and β^* shown in Table I, we can plot ΔG and ΔH with respect to the stress, presented in Fig. 12. The difference between the Gibbs free energy and the enthalpy is related to the entropic factor, which is relatively small for the range of stresses shown in the figure. This implies that the bias expected from using HTST will be moderate, mostly at stress lower than 300 MPa. We will take advantage of this fact for the development of a KMC approach to study twin thickening rates.

3. Object kinetic Monte Carlo model for twin growth

In order to quantify the respective and collective contributions of each interfacial defect (i.e., KP height) to the kinetics
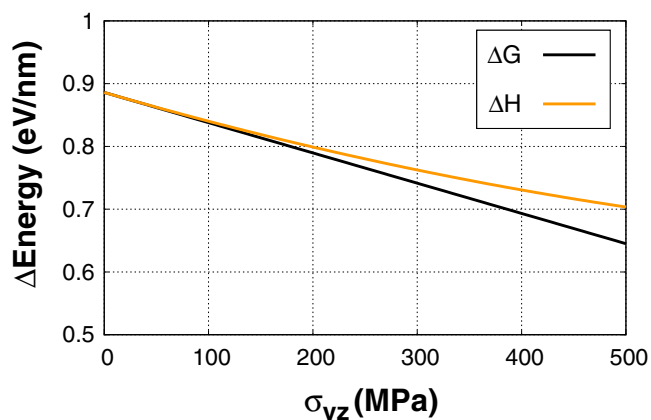

FIG. 12. ΔG and ΔH as a function of stress as given by the fit to MD data.

TABLE I. Fitted values of the parameters in Eq. (17) to MD data.

K (ps^{-1} MPa^{-1} nm^{-1})	α	δ	ΔF (eV/nm)	v_a^* (nm^3/nm)	β^* (nm^3/nm^{-1} MPa^{-1})
1.122×10^5	0.11	3.217	0.886	0.077	4.42×10^{-5}

of twin thickening, a KMC framework has been developed. The KMC algorithm solves for the dynamic evolution of a given system provided that the rates of every possible event are known. In that case, the KMC will result in the correct time evolution for the model used, providing one realization for the master equation [33–35]. We propose here a rather simple physical model to study twin thickening in two dimensions, sketched in Fig. 13. We first discretize the twin boundary in small segments of length $b_{2/2}$, inspired by, for example, discrete dislocation dynamics algorithms [36,37]. Each segment has a rate to move forward (positive z's) or backward (negative z's) and only one segment moves per time step. These rates are calculated according to HTST by the expression $\Gamma = \nu_0 \exp\left(-\frac{\Delta E - \sigma_{yz} v_a}{kT}\right) = \nu_0 \exp\left(-\frac{\Delta H}{kT}\right)$. The ΔH is approximated through a pair interaction model by which each segment interacts just with its first nearest neighbors,

$$\Delta H = \Delta H_0^{(+/-)}(\sigma) + \sum_n g_n(\sigma, \Delta z)\Delta z. \quad (20)$$

$\Delta H_0^{(+/-)}(\sigma)$ is the enthalpy barrier for nucleation (or Peierls barrier) of a minimum width KP from a flat interface as given by NEB (see Fig. 5). The applied stress modifies the energy landscape, altering both the barriers for the segment to nucleate toward positive z's and negative z's (see Fig. 13). The Peierls barrier upon migration forward [$\Delta H_0^+(\sigma)$] is taken as the one given by NEB, while the one for the direction backwards has been obtained relying on a linear approximation such that $\Delta H_0^-(\sigma) = 2\Delta H_0(0) - \Delta H_0^+(\sigma)$, with $\Delta H_0(0) = 0.721$ eV/nm the enthalpy barrier at zero stress. These nucleation barriers will be taken as reference, and will be modified depending on the position of the first nearest neighbor segments to give the final enthalpy barrier for a given configuration. Δz is the distance between segments in the z direction and $g_n(\sigma, \Delta z)$ are the pair interactions that depend on the applied stress σ and Δz. These pair interactions have been fitted to reproduce the barriers obtained with NEB along with the twin growth rate obtained from MD. The values used in this study are shown in Table II. The pre-exponential factor that better fits the MD values is $\nu_0 = 9.0 \times 10^{-1}$ ps^{-1}. The strain at each timestep is

calculated as $\epsilon_{yz} = b_{2/2}\langle\Delta z\rangle/L_z$ and the slope of the strain with respect to time is taken as the strain rate.

The efficiency of this model allows us to explore different external conditions without much computational burden. Following this methodology we have computed the twin growth rate for stresses ranging from 100 to 500 MPa and temperatures from 100 to 700 K. Figure 14(a) shows a map of the rates obtained, which are indeed comparable to the ones obtained from MD simulations [see Fig. 10(c)]. We note that the rates are monotonic with low and high rates at low and high temperatures and stresses, respectively. At high temperatures and stresses, the validity of HTST starts to be questionable and thus the actual rates might differ from those obtained with our KMC model. Nevertheless, the results should provide an estimate of the orders of magnitude expected under a set of external conditions.

Finally, the use of the KMC method allows one to assess the morphology of the interface between the twin and parent domains as a function of temperature and stress. Figure 14(b) shows an example at a shear stress $\sigma_{yz} = 100$ MPa, where the interface elements are plotted for 300 and 700 K. We note that the interface is rougher at 700 K with larger kinks corresponding to B/P interfaces. Although admittedly limited, mostly due to the lack of long-range interactions, the results from the KMC approach follow the same trends as the MD data, Figs. 10(c) and 14(a).

IV. CONCLUSIONS

In this work, we have analyzed in detail the properties of the B/P interfaces forming a kink pair (KP) of growing $\{10\bar{1}2\}\langle\bar{1}011\rangle$ twins in α-Ti. Using atomistic modeling, it was observed that the interaction energy between kinks follows a logarithmic law and varies with applied shear stress, but not with normal stress. The core energy of $b_{2/2}$ disconnections was calculated and found to be $E_{b2/2}^{core} = 0.188$ eV/nm. Pure bending seems to do work when curvature is applied to the system, which lowers the formation energy and raises questions about the nature of the interface defects at the kinks. We found that the stability of the KPs depends on their width
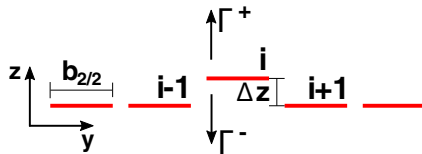

FIG. 13. Discretization model used in the KMC simulations. The twin segments are shown in read, each of length $b_{2/2}$. The rates for segment i to go forward (Γ^+) or backwards (Γ^-) depend on the position of the segment i and its first nearest neighbors, ($i - 1$ and $i + 1$). The hoping length of the segments in the z direction is normalized to $2d_{\{10\bar{1}2\}}$.

TABLE II. $\Delta H_0^+(\sigma)$ and $\Delta H_0^-(\sigma)$ in eV (for a kink length of 0.295 nm) and the interaction parameters $g_n(\sigma, \Delta z)$ in eV/$2d_{\{10\bar{1}2\}}$. $2\cdots$ and $-2\cdots$ stands for the fact that the value is the same for $\Delta z \geqslant 2$ and $\Delta z \leqslant -2$, respectively. Shear stresses in MPa are given in the first column.

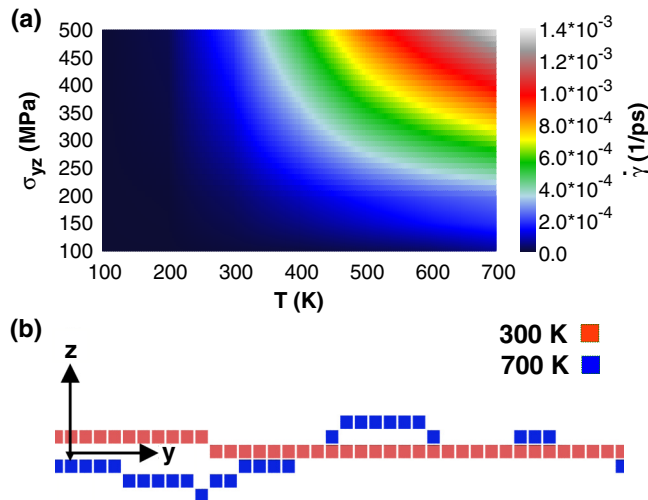| σ	$\Delta H_0^+(\sigma)$	$\Delta H_0^-(\sigma)$	$g(\sigma, 1)$	$g(\sigma, 2\cdots)$	$g(\sigma, -1)$	$g(\sigma, -2\cdots)$
100	0.204	0.222	−0.194	−0.110	0.177	0.101
150	0.197	0.229	−0.201	−0.113	0.172	0.098
200	0.195	0.231	−0.201	−0.114	0.172	0.097
500	0.176	0.250	−0.150	−0.119	0.154	0.087

FIG. 14. (a) Strain rate map as obtained with the KMC model for different stress and temperature conditions. (b) Snapshots of the twin interfaces at $\sigma_{yz} = 100$ MPa and 300 (red) and 700 K (blue) to show the different roughness depending on the temperature.

and height for a given shear stress: the further apart the kinks the higher the most stable KP. We have developed a twin thickening model based on thermally activated glide descriptions that reduces to a previous model available in the literature [30] when the kink propagation rate is much larger than the nucleation rate. We have tested the theoretical expressions with results from MD simulations with satisfactory agreement. We note that transition state theory (TST) holds in the studied stress range. However, its harmonic approximation deviates slightly from the TST rates beyond intermediate stresses ($\gtrsim$ 200 MPa). Finally, we have developed a kinetic Monte Carlo model to study twin growth that allows us to analyze diverse external conditions without much computational burden. The theoretical results obtained in this work imply a high mobility of the B/P interfaces and therefore a large twin growth rate, which correlates qualitatively with experimental observations.

[1] B. A. Bilby and A. G. Crocker, The theory of the crystallography of deformation twinning, Proc. R. Soc. London A **288**, 240 (1965).

[2] J. W. Christian and S. Mahajan, Deformation twinning, Prog. Mater. Sci. **39**, 1 (1995).

[3] J. P. Hirth and R. C. Pond, Steps, dislocations and disconnections as interface defects relating to structure and phase transformations, Acta Mater. **44**, 4749 (1996).

[4] A. Serra and D. J. Bacon, A new model for {10-12} twin growth in hcp metals, Philos. Mag. A **73**, 333 (1996).

[5] A. Staroselsky and L. Anand, A constitutive model for hcp materials deforming by slip and twinning, Int. J. Plast. **19**, 1843 (2003).

[6] J. Hirth, R. Pond, R. Hoagland, X.-Y. Liu, and J. Wang, Interface defects, reference spaces and the Frank–Bilby equation, Prog. Mater. Sci. **58**, 749 (2013).

[7] J. Hirth, J. Wang, and C. N. Tomé, Disconnections and other defects associated with twin interfaces, Prog. Mater. Sci. **83**, 417 (2016).

[8] J. Wang, J. Hirth, and C. N. Tomé, (10$\bar{1}$2) twinning nucleation mechanisms in hexagonal-close-packed crystals, Acta Mater. **57**, 5521 (2009).

[9] R. C. Pond, J. P. Hirth, A. Serra, and D. J. Bacon, Atomic displacements accompanying deformation twinning: shears and shuffles, Mater. Res. Lett. **4**, 185 (2016).

[10] Q. Yu, J. Wang, Y. Jiang, R. J. McCabe, N. Li, and C. N. Tomé, Twin–twin interactions in magnesium, Acta Mater. **77**, 28 (2014).

[11] Q. Yu, J. Wang, Y. Jiang, R. J. McCabe, and C. N. Tomé, Co-zone {10$\bar{1}$2} twin interaction in magnesium single crystal, Mater. Res. Lett. **2**, 82 (2014).

[12] H. E. Kadiri, C. D. Barrett, J. Wang, and C. N. Tomé, Why are {10-12} twins profuse in magnesium? Acta Mater. **85**, 354 (2015).

[13] L. Leclercq, L. Capolungo, and D. Rodney, Atomic-scale comparison between {−1101} and {−1102} twin growth mechanisms in magnesium, Mater. Res. Lett. **2**, 152 (2014).

[14] M. Y. Gong, G. Lin, J. Wang, L. Capolungo, and C. N. Tomé, Atomistic simulation of basal dislocation and twin interactions in Mg (unpublished).

[15] A. Ostapovets and A. Serra, Characterization of the matrix-twin interface of a (10-22) twin during growth, Philos. Mag. **94**, 2827 (2014).

[16] A. Ostapovets, J. Bursik, and R. Groger, Deformation due to migration of faceted twin boundaries in magnesium and cobalt, Philos. Mag. **95**, 4106 (2015).

[17] M. Gong, J. P. Hirth, Y. Liu, Y. Shen, and J. Wang, Interface structures and twinning mechanisms of twins in hexagonal metals, Mater. Res. Lett. **5**, 449 (2017).

[18] M. A. Meyers, O. Vöhringer, and V. A. Lubarda, The onset of twinning in metals: a constitutive description, Acta Mater. **49**, 4025 (2001).

[19] M. Barnett, C. Davies, and X. Ma, An analytical constitutive law for twinning dominated flow in magnesium, Scr. Mater. **52**, 627 (2005).

[20] A. Jain and S. Agnew, Modeling the temperature dependent effect of twinning on the behavior of magnesium alloy AZ31B sheet, Mater. Sci. Eng., A **462**, 29 (2007).

[21] G. Henkelman, B. P. Uberuaga, and H. Jonsson, A climbing image nudged elastic band method for finding saddle points and minimum energy paths, J. Chem. Phys. **113**, 9901 (2000).

[22] S. Plimpton, Fast parallel algorithms for short-range molecular dynamics, J. Comput. Phys. **117**, 1 (1995).

[23] M. I. Mendelev, T. L. Underwood, and G. J. Ackland, Development of an interatomic potential for the simulation of defects, plasticity, and phase transformations in titanium, J. Chem. Phys. **145**, 154102 (2016).

[24] O. MacKain, M. Cottura, D. Rodney, and E. Clouet, Atomic-scale modeling of twinning disconnections in zirconium, Phys. Rev. B **95**, 134102 (2017).

[25] M. Dupeux and R. Bonnet, Stresses, displacements and energy calculations for interfacial dislocations in anisotropic two-phase media, Acta Metall. **28**, 721 (1980).

[26] C. Fressengeas, V. Taupin, and L. Capolungo, An elasto-plastic theory of dislocation and disclination fields, Int. J. Solids Struct. **48**, 3499 (2011).

[27] D. Cereceda, M. Diehl, F. Roters, D. Raabe, J. M. Perlado, and J. Marian, Unraveling the temperature dependence of the yield strength in single-crystal tungsten using atomistically-informed crystal plasticity calculations, Int. J. Plast. **78**, 242 (2016).

[28] G. Po, Y. Cui, D. Rivera, D. Cereceda, T. D. Swinburne, J. Marian, and N. Ghoniem, A phenomenological dislocation mobility law for bcc metals, Acta Mater. **119**, 123 (2016).

[29] M. Gilbert, S. Queyreau, and J. Marian, Stress and temperature dependence of screw dislocation mobility in α-Fe by molecular dynamics, Phys. Rev. B **84**, 174103 (2011).

[30] A. Luque, M. Ghazisaeidi, and W. A. Curtin, A new mechanism for twin growth in Mg alloys, Acta Mat. **81**, 442 (2014).

[31] E. Martinez, D. Perez, V. Gavini, and S. Kenny, Advanced atomistic algorithms in materials science, J. Mat. Res. **33**, 773 (2018).

[32] U. F. Kocks, A. S. Argon, and M. F. Ashby, Thermodynamics and kinetics of slip, Prog. Mat. Sci. **19**, 1 (1975).

[33] A. B. Bortz, M. H. Kalos, and J. L. Lebowitz, A new algorithm for Monte Carlo simulation of Ising spin systems, J. Comput. Phys. **17**, 10 (1975).

[34] D. Gillespie, A general method for numerically simulating the stochastic time evolution of coupled chemical reactions, J. Comput. Phys. **22**, 403 (1976).

[35] D. Gillespie, Exact stochastic simulation of coupled chemical reactions, J. Phys. Chem. **81**, 2340 (1977).

[36] A. Arsenlis, W. Cai, M. Tang, M. Rhee, T. Oppelstrup, G. Hommes, T. G. Pierce, and V. V. Bulatov, Enabling strain hardening simulations with dislocation dynamics, Modelling Simul. Mater. Sci. Eng. **15**, 553 (2007).

[37] A. Stukowski, D. Cereceda, T. D. Swinburne, and J. Marian, Thermally-activated non-Schmid glide of screw dislocations in W using atomistically-informed kinetic Monte Carlo simulations, Int. J. Plast. **65**, 108 (2015).